ARTICLE IN PRESS

Journal of Manufacturing Systems xxx (xxxx) xxx–xxx

Contents lists available at ScienceDirect

Journal of Manufacturing Systems

journal homepage: www.elsevier.com/locate/jmansys

Monitoring temperature in additive manufacturing with physics-based compressive sensing

Yanglong Lu, Yan Wang*

Woodruff School of Mechanical Engineering, Georgia Institute of Technology, United States

ARTICLE INFO

Keywords:
Additive manufacturing
Compressed sensing
Process monitoring
Temperature distribution

ABSTRACT

Sensing is one of the most important components in manufacturing systems to ensure the high quality of products. However, the deployment of a large number of sensors increases the costs of manufacturing systems for both operation and maintenance. Processing the large amount of sensor data for real-time process monitoring is also challenging. Recently compressive sampling or compressed sensing (CS) approaches have been developed to reduce the amount of data collection. However, the reduction is limited to individual sensor types and compression ratio is not high. In this paper, a physics-based compressive sensing (PBCS) approach is proposed to improve the traditional CS approach based on the physical knowledge of phenomenon in applications. The volume of data and the number of sensors needed for process monitoring are significantly reduced. This approach is applied to monitor the temperature field of additive manufacturing processes. In the experimental study, only a few number of thermal readings are needed to reconstruct the complete three-dimensional temperature field using the PBCS approach.

1. Introduction

Sensors have become indispensable for increasingly complex manufacturing processes to ensure high quality of products. In many cases, the process becomes so complex that it completely relies on in-situ sensors to provide online monitoring. There are two major challenges for the "sensor dependency". The first one is the life-cycle cost of sensors. The cost portion of sensing system installation, operation, and maintenance in the overall cost of manufacturing is rising. More importantly, the reliability of sensors will easily become the weakest link of the reliability of complex systems with a large number of sensors onboard. As a result, the maintenance cost of sensing subsystems is likely to be a major portion of system life-cycle costs. Furthermore, undetected faulty sensors provide inaccurate information and can lead to costly wrong decisions. The second challenge is the bandwidth limitation of communication for the volume of data to be transmitted to enable remote monitoring, diagnostics, and control. Although sensor technologies will gradually become more affordable, communication channels will always be the bottleneck to realize industrial scale Internet of Things or Industry 4.0, where the large volume of data being constantly generated can be easily wasted without being shared in time and used for their original purposes of control and decision making. The scalability of sensor networks as the number of sensors rapidly grows is a major issue of the emerging intelligent and advanced manufacturing systems.

Given the above challenges of applying large-scale and ubiquitous sensing systems in manufacturing, can we develop new protocols to collect and share information more efficiently without relying on current practice of "what you see is what you collected"? More specifically, can we obtain high-fidelity information from the data collected with low-fidelity low-cost sensing systems without deploying a large number of high-resolution high-end sensors? There is a practical need of deploying the minimum number of sensors to effectively monitor system performance. Reducing the number of sensors can improve the cost-effectiveness for system monitoring and control. Reducing the amount of data in communication without sacrificing the amount of information exchanged will also enable us to build scalable sensing and communication networks.

In the most recent decade, a new sampling and data collection approach, compressive sampling or compressed sensing (CS), was developed. CS is a new approach to generate a signal by taking advantage of sparsity so that the amount of collected data can be largely reduced. The main idea is to collect a small set of samples and recover the original signal computationally from these samples. More specifically, if the signal can be represented in the reciprocal space with only a small number of coefficients through transformation, e.g. Fourier and wavelet transforms, then when the signal is projected linearly into a different space with a much lower dimension, the original signal can be

* Corresponding author at: 801 Ferst Drive NW, Atlanta, GA 30332-0405, United States.
E-mail address: yan.wang@me.gatech.edu (Y. Wang).

https://doi.org/10.1016/j.jmsy.2018.05.010
Received 28 December 2017; Received in revised form 19 May 2018; Accepted 21 May 2018
0278-6125/

recovered, even without much knowledge of projection. The recovery can be fairly precise when the number of non-zero coefficients in the reciprocal space is small (i.e. *sparse*) and the transformation and projection operations are not correlated (i.e. *incoherent*).

Different from traditional CS techniques developed for generic one- or two-dimensional (2D) signals without the consideration of application domains, which are pure data-driven approaches, here a physics-based compressive sensing (PBCS) approach is proposed, which relies on the domain knowledge of specific applications. It is believed that the physical knowledge of the phenomenon that we would like to observe can potentially help us to design more efficient and accurate compressive sensing protocols.

If the original signal has a size of N and its representation in the reciprocal space is sparse with only K non-zero coefficients ($K < N$), standard CS for generic signals allows for robust recovery from $M = O(K\log(N/K))$ measurements. That is, with M measured data points in the order of $K\log(N/K)$, the original data with size N can be recovered. The compression ratio is N/M. The latest development for images (i.e. 2D signals) has reduced M further to $M = O(K)$.

In this paper, we will demonstrate that the proposed PBCS can significantly further improve the compression ratio based on the physical knowledge of the system. Here, the generic PBCS formalism is proposed and applied to monitor the temperature distribution in additive manufacturing (AM) process. In AM processes such as powder bed fusion and material extrusion, materials are locally heated, melt, and solidified to build free-form geometries layer-by-layer. Material phase transition processes (sintering, melting, crystallization, solidification, etc.) are critically dependent on the spatial temperature distribution and its temporal evolution. Therefore, controlling the temperature distribution in the materials is one of the most important factors to ensure the build quality in AM.

The novelty of the proposed PBCS is that it significantly improves compression ratio from traditional CS by incorporating the prior knowledge of physical quantities to be monitored. It is shown that a 3D temperature field can be monitored by the reconstruction from only a few number of single-probe thermal readings. The compression ratio can be improved by two orders of magnitude from the traditional CS with the similar accuracy.

In the remainder of the paper, the background of CS, its application in machine condition monitoring, and inverse heat transfer problem is given in Section 2. The generic framework of PBCS is proposed in Section 3. The setup of experiments for demonstration is described in Section 4. The applications of PBCS in 2D and 3D temperature field reconstructions are demonstrated in Section 5.

2. Background

2.1. Compressed sensing or compressive sampling (CS)

Compressed sensing or compressive sampling [1,2] was initially developed to solve the inverse problem of information recovery purely based on statistical characteristics of signals. Suppose that the original signal is represented in a discrete format as vector. It can be represented in the reciprocal space via transformation as $\boldsymbol{s} = \boldsymbol{\Psi\alpha}$ where $\boldsymbol{\Psi}$ is the matrix representation of transformation (or basis matrix) and $\boldsymbol{\alpha}$ is the vector of coefficients. The size of the original signal vector $\boldsymbol{s}$ is N. The size of the coefficients $\boldsymbol{\alpha}$ could be similar to N, however, only K of them are non-zero ($K < N$). That is, $\boldsymbol{\alpha}$ is K-sparse. When the signal is projected into another space to $\boldsymbol{y} = \boldsymbol{\Phi s}$ with a reduced dimension M ($M < N$) via a projection (or measurement) matrix $\boldsymbol{\Phi}$. The recovery of the original signal from the measured data is to solve the linear equations $\boldsymbol{y} = \boldsymbol{\Phi s} = \boldsymbol{\Phi\Psi\alpha} = \boldsymbol{\Theta\alpha}$. Loosely speaking, because of the K-sparsity, solving $\boldsymbol{\Theta\alpha} = \boldsymbol{y}$ first to find $\boldsymbol{\alpha}$ then reconstructing the original signal by $\boldsymbol{s} = \boldsymbol{\Psi\alpha}$ provides more accurate recovery than solving $\boldsymbol{\Phi s} = \boldsymbol{y}$ to find $\boldsymbol{s}$ directly. CS has been extensively applied in signal processing [3,4], image processing [5,6,7], networked sensing [8], and others.

Various solving procedures for CS problems have been developed. These approaches include convex relaxation (e.g. basis pursuit (BP) [9], LASSO [10], LARS [11], nuclear norm minimization [12]), greedy iteration algorithms (e.g. matching pursuit [13], orthogonal matching pursuit (OMP) [14], regularized OMP [15], stagewise OMP [16], CoSaMP [17], subspace pursuit [18], gradient projection [19], orthogonal multiple matching pursuit [20]), iterative thresholding algorithms (e.g. soft thresholding [21], hard thresholding [22], sparse recovery [23], sequential sparse matching pursuit [24]), combinatorial and sublinear algorithms (e.g. Fourier sampling algorithm [25], HHS [26]), non-convex minimization (e.g. [27], FOCUS [28], iterative regularization algorithm [29], and others.

2.2. Application of classical CS in machine condition monitoring

Recently, CS started being used to monitor machine health conditions. Chen et al. [30] used it to extract impulse components of roller bearing vibration signals. Wang et al. [31] applied to time-frequency sparse representation of gear box vibration signals. Wang et al. [32] applied it to down sampling of bearing vibration signals. Tang et al. [33] classified the faults of rotating machinery with compressed measurements. Ding and He [34] applied to noise removal in the time-frequency domain. Yuan and Lu [35] applied CS to identify the health states of rolling bearing based on compressed vibration signals. Liu et al. [36] demonstrated the feasibility of using compressed features to identify rolling bearing states from acoustic emission signals.

To improve the performance, researchers also trained and optimized the basis/transformation matrix so that higher sparsity of the reciprocal coefficients can be achieved. The training process was also called the dictionary learning, which has been based on the maximum likelihood [30], least-square error [37,34], and hidden Markov model [38].

All of the above approaches applied classical data-driven CS to machine condition monitoring. Signals were generally treated in the same way as any other type of data without the consideration of domain specific knowledge.

2.3. Inverse heat transfer problem

Here the proposed PBCS is to reconstruct temperature distributions from limited measurements by solving the inverse problem. Some limited efforts have been given to study the inverse heat transfer problem [39], which is to estimate unknown quantities including boundary conditions of radiation [40] and convection [41,42], thermophysical properties, initial condition, source terms, and geometry [43] of a heated body with transient temperature measurements. Generic optimization techniques such as adjoint local search, conjugate gradient method [44], genetic algorithm [45] have been applied. The performance of these methods is sensitively dependent on the number of unknown parameters to be estimated. Excursion and oscillation of the solution may occur when the number of parameters is large.

In contrast, the proposed PBCS relies on the sparsity of the coefficient vector in the sense of CS to solve the inverse problem. If the vector to be recovered has a high level of sparsity, it is shown that CS can be very efficient and also provide very accurate results. In PBCS formulation, the knowledge of physical models is used to identify the sparsity that is inherent in the models, such as boundary conditions in heat transfer problems so that PBCS can take advantage of sparsity for robust reconstruction.

3. Proposed PBCS mechanism

The proposed PBCS approach is to reduce the operational cost of the sensing system by using low-fidelity measurements to obtain high-fidelity information, for example, using single probe based measurements (e.g. thermocouple, or noncontact pyrometer) to measure the complete temperature distribution, or using the low-resolution thermal infrared imaging to obtain the high-resolution thermal distribution.

The idea of PBCS is to combine limited or low-fidelity experimental measurements with predictions from physics-based models to numerically reconstruct high-fidelity measurement information. In Section 3.1, the generic framework of PBCS is described. The physical models serve as the constraints in the information recovery process. In Section 3.2, the generic PBCS framework is demonstrated with the case of temperature distribution measurements, which is based on a heat transfer model.

3.1. Generic PBCS framework

The recovery of original information from the collected data is to solve the inverse problem

$$\min \| \boldsymbol{\alpha} - \boldsymbol{\alpha}_0 \|_{l_p} \ (p = 0, 1, 2)$$
$$\text{subject to} \quad \boldsymbol{y} = \boldsymbol{f}(\mathrm{t}, \boldsymbol{\alpha}, \boldsymbol{y}, \dot{\boldsymbol{y}}, \ddot{\boldsymbol{y}}, \nabla \boldsymbol{y}, \ldots) \tag{1}$$

where $\boldsymbol{f}$ are functions of time t, coefficients or model parameters $\boldsymbol{\alpha}$ that need to be recovered, measurements $\boldsymbol{y}$, as well as their time or space derivatives ($\dot{\boldsymbol{y}}$, $\ddot{\boldsymbol{y}}$, $\nabla \boldsymbol{y}$, ...). Note that the physics of phenomena is modeled by $\boldsymbol{f}$ in Eq. (1), which is different from traditional CS that only relies on linear projection and transformation without physical models. The minimization can be based on the criteria of l_0, l_1, or l_2 norm.

The proposed PBCS captures generic physical phenomena. For a system described by partial differential equations (PDEs), the recovery is a PDE-constrained optimization problem. If system dynamics is to be monitored, the constraining physical models will be ordinary differential equations (ODEs). The simplest case is when the constraints are just linear equations, which have a format that is similar to classical CS but are associated with more physical meanings.

The generality of PBCS lies in its generic mathematical framework of introducing physical models into the original inverse problem of CS. Therefore, the physical knowledge of the system can help accelerate the inference process.

3.2. Thermal PBCS for temperature field measurement

Here a model for the temperature distribution measurement and reconstruction is used to illustrate the proposed PBCS framework and the procedure of building domain specific PBCS from the generic framework. Temperature is one of the most important process parameters to monitor and control in many manufacturing processes. Temperature distributions in the domains of materials and processing environments determine final properties of products, especially for those experiencing phase transformation or transition such as grain growth, defect propagation, deposition, and solidification.

In PBCS formulation, the characteristics of temperature field T can be generally described by the PDE for local balance in domain Ω as

$$c_V \frac{dT}{dt} - \kappa \nabla \cdot (\nabla T) - Q = 0 \quad \text{in} \quad \Omega \tag{2}$$

where c_V is the specific heat at constant volume, κ is the thermal conductivity, and Q is the rate of heat generation per unit volume. For a static system at equilibrium, the time derivative becomes zero. Eq. (2) is simplified to

$$\kappa \nabla \cdot (\nabla T) + Q = 0 \quad \text{in} \quad \Omega \tag{3}$$

If boundary conditions such as heat flux and convection are applied in the subdomain $\partial\Omega$, a balance of energy transferred across the boundary can be expressed as

$$\kappa \nabla T \bullet \hat{n} + h_c (T - T_\infty) = g \tag{4}$$

where h_c is the heat transfer coefficient for thermal convection, T_∞ is the ambient temperature, g is the heat flux and $\hat{n}$ donates the unit normal vector to the boundary. With test function w, the weak form of Eq. (3) is

$$\int_\Omega (\kappa \nabla w \nabla T - wQ) d\Omega - \int_{\partial\Omega} (w\kappa \nabla T \bullet \hat{n}) d(\partial\Omega) = 0 \tag{5}$$

The temperature field can be approximated with finite-element alike formulation. With the consideration of boundary conditions by plugging Eq. (4) to Eq. (5) and given finite element basis functions δ_i' s, the discretized formulation is

$$\mathbf{K}_s \boldsymbol{T} = \boldsymbol{L} \tag{6}$$

where

$$\mathbf{K}_s = \{\int_\Omega \kappa \nabla \delta_i \bullet \nabla \delta_j \, d\Omega\} + \{\int_{\partial\Omega} h_c \delta_i \bullet \delta_j \, d(\partial\Omega)\}$$

is the conduction matrix and

$$\boldsymbol{L} = \{\int_\Omega Q\delta_i \, d\Omega\} + \{\int_{\partial\Omega} g\delta_i \bullet d(\partial\Omega)\} + \{\int_{\partial\Omega} h_c T_\infty \delta_i \bullet d(\partial\Omega)\}$$

is the heat load vector.

The original PBCS problem, which is a PDE-constrained optimization under constraint in Eq. (3), is converted to

$$\min \|\boldsymbol{y} - \boldsymbol{\Phi T}\|_{l_p} (p = 0, 1, 2)$$
$$\text{subject to} \quad \boldsymbol{y} = \boldsymbol{\Phi T} = \boldsymbol{\Phi} \boldsymbol{K}_s^{-1} \boldsymbol{L} \tag{7}$$

based on some l_p-norm criteria, where $\boldsymbol{L}$ can be recovered from the measurements $\boldsymbol{y}$, which is a small portion of the complete temperature field $\boldsymbol{T}$. Then the temperature field can be reconstructed as $\boldsymbol{T} = \mathbf{K}_s^{-1} \boldsymbol{L}$.

4. Experimental setup

A Hyrel 3D printer was used in the experiment to print a simple box with the size of 45 mm × 45 mm × 6 mm. The material was acrylonitrile butadiene styrene (ABS). The typical approach to monitor the temperature distribution is using thermal imaging systems. During the printing process, a Seek thermal camera was used to capture the grayscale image of the temperature field, which is shown in Fig. 1(a). Particularly, the temperature distribution at the top surface of the print is the domain of interest and is used to assess the PBCS accuracy.

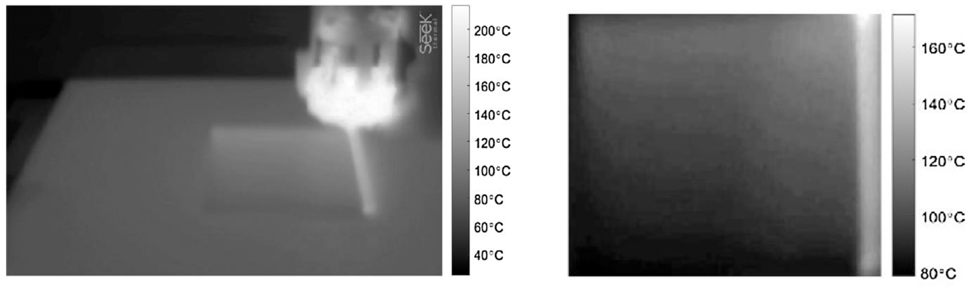

(a) (b)

Fig. 1. Thermal image captured with the Seek thermal camera. (a) Original thermal image; (b) Processed image after converting pixel values to temperatures.

Since the view angle of the experimentally captured image for the domain is different from a rectangular 2D image, an image registration process was performed to map the domain to a regular image. The right edge of the domain is the newly printed line segment with the highest temperature values. Thus the right edge was used as a reference feature in image registration. The image registration tool in Matlab was used. Affine transformations including translation, rotation, scaling, and shearing were applied to the experimentally captured image. After image registration, the image was scaled to 45 × 45 pixels. Each pixel in the gray-scale image was converted to a temperature scale with a linear map, where the temperature was derived from the pixel value with a linear interpolation between the minimum and maximum temperatures and rounded to the nearest integer. The processed image with each pixel value as the actual temperature is shown in Fig. 1(b). The temperature distribution on the top surface of the printed part is used to compare with PBCS reconstruction in Section 5.2.

A second experiment was conducted with the consideration of temperature changes in the cooling process. With the same procedure of image processing and registration, the experimentally measured temperature fields at time 0 s, 4 s and 8 s after the printer was paused are shown in Fig. 2(a)–(c) respectively, and the corresponding images after registration in Fig. 2(d)–(f). The demonstration of PBCS for the cooling process monitoring is described in Section 5.3.

5. Thermal PBCS to monitor additive manufacturing process

In this section, a simple 2D thermal model of the material extrusion process is first used to illustrate the proposed PBCS approach in Section 5.1. Sensitivities of measurement strategies are also analyzed. Then a PBCS based 3D temperature distribution monitoring is used to demonstrate the new sensing method in Sections 5.2 and 5.3.

5.1. 2D thermal model

A 2D physical model of material extrusion is constructed, as illustrated in Fig. 3, where one quarter of the printing area is modeled. The extruder as the heat source is located at the bottom left corner of the domain without movement, and the top and right boundaries correspond to the hotbed temperature. 88 quadratic triangular elements are used in the discretized finite-element formulation, with a total of 205 nodes in the 2D domain. Following the regular finite element modeling, a heat load vector is assigned, and the temperature distribution predicted from the model is used as the reference for comparison. During

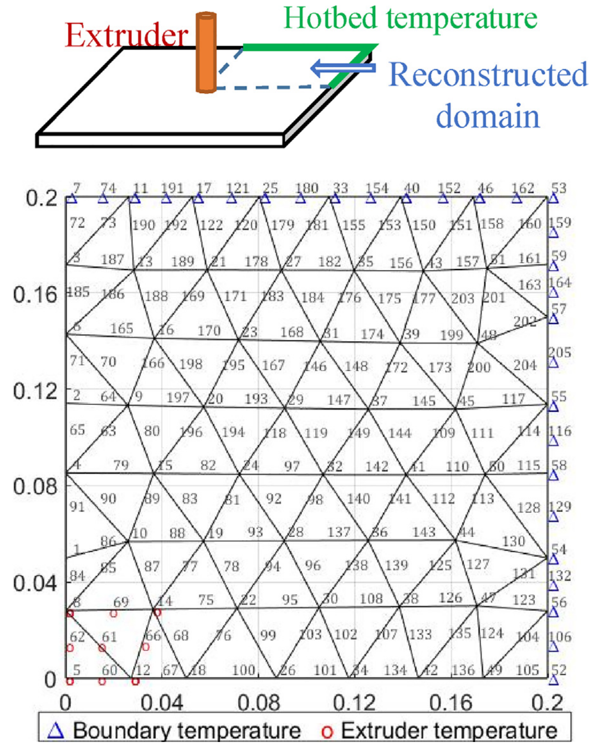

Fig. 3. 2D finite-element domain of temperature distribution in °C for reconstruction.

PBCS, some nodal temperatures are selected and treated as if they were measurements. They are then used to recover the heat load vector. The recovered heat load vector is employed to reconstruct the temperature distribution, which is compared with the original one. The purpose of not taking measurements directly from the actual physical experiments is to illustrate the PBCS error associated with recovery algorithms without the confounding effect of measurement errors in physical experiments. Two cases are studied. In the first case, only temperatures of the extruder and the hotbed are sampled, denoted by circles and triangles respectively. In the second case, temperature samples are taken at the boundary and a few locations inside the domain.

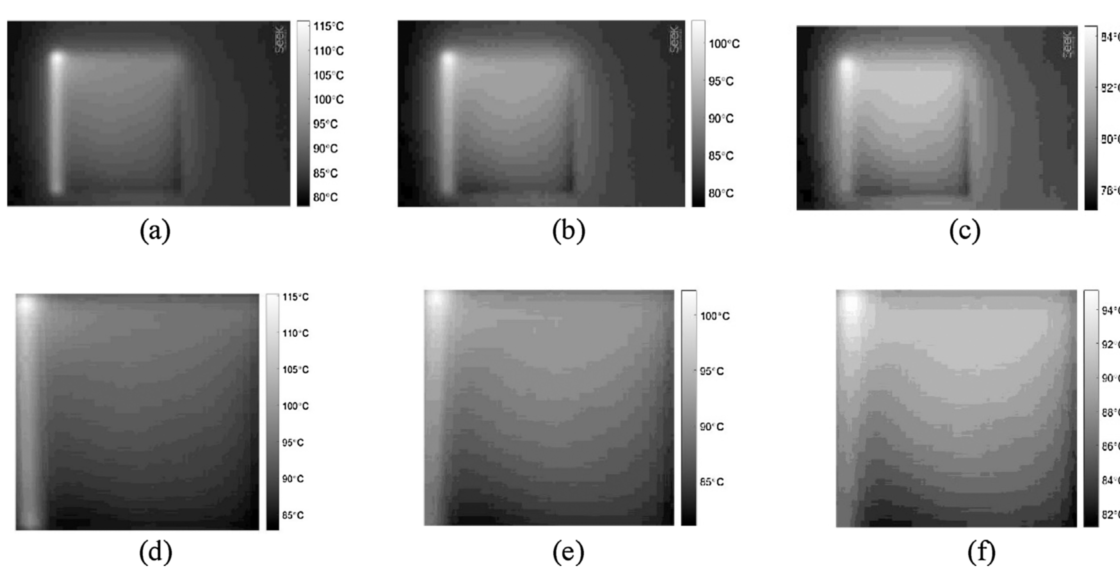

Fig. 2. Measured temperature distributions in the cooling process at time (a) 0 s, (b) 4 s, and (c) 8 s as well as the corresponding images after registration in (d)–(f).

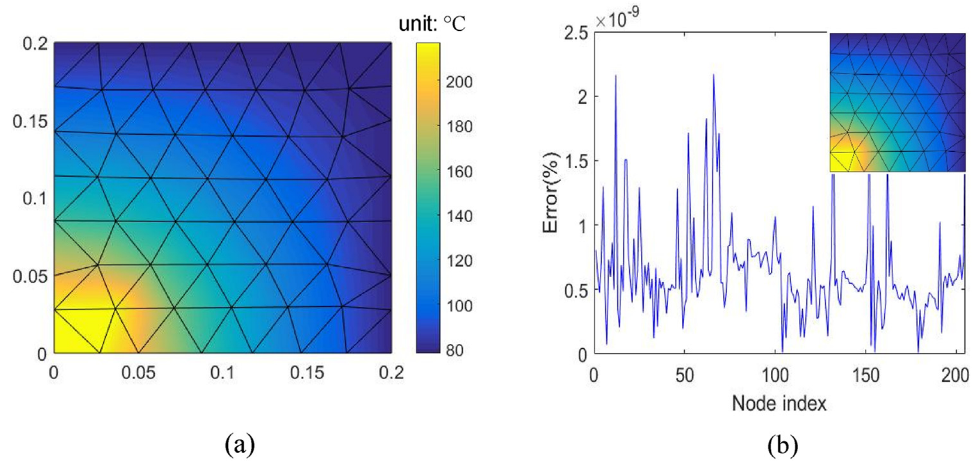

Fig. 4. Reconstruction of 2D temperature distribution. (a) Original temperature distribution from the finite-element model; (b) Reconstruction error at the all nodal positions with the basis pursuit algorithm.

5.1.1. *Case 1: single-probe measurements at extruder and hotbed*

Fixed temperature boundary conditions are applied to the top- and right-side of the domain (hotbed) and the bottom-left corner (extruder). It is reasonable to assume that all 29 nodes at the top- and right-side boundaries have the same temperature of hotbed, which is 78 °C, whereas 9 nodes on the bottom-left corner have the same temperature of extruder, which is 217 °C. The sparse heat load vector $\boldsymbol{L}$ is first recovered from temperatures at these 38 nodes**.** Then all nodal temperatures $\boldsymbol{T}$ in Eq (7) are reconstructed. After the heat load vector is recovered, those values in the vector that are smaller than a threshold of 10^{-5} are set to be zeros to eliminate the numerical round-off effect. The PBCS reconstructed temperature is the same as the original one from the finite element model in Fig. 4(a). The differences between temperatures of all 205 nodes based on the basis pursuit algorithm [9] are shown in Fig. 4(b). The reconstructions are exact, and the heat load vector can be lossly recovered.

5.1.2. *Case 2: low-fidelity measurement inside printing domain and hotbed*

The measurement matrix $\mathbf{\Phi}$ in Eq. (7) contains the indices of nodes in the model, which indicate the locations where the temperatures need to be measured. Choosing different locations of measurements may result in different levels of reconstruction accuracy.

In the measurement strategy shown in Fig. 5(a), instead of measuring the extruder temperature, some internal temperatures within the domain are used and the locations are highlighted with stars (*). This strategy can be regarded as measurements from pyrometers at various locations. The hotbed temperature is also used for reconstruction. A total of 48 nodal temperatures, including 19 internal nodes and 29 nodes at the top- and right-side boundaries, are used for recovery. The boundary condition of the physical model is changed with heat flux at extruder nodes. Fig. 5(b) shows the reconstruction results and errors. The errors are larger than the ones in Fig. 4(b). If the internal measurements are concentrated in a local region, which can be regarded as the case where the infrared camera measures a portion of the domain, as shown in Fig. 5(c), the reconstruction results are different, as shown in Fig. 5(d), where errors further increase from the ones in Fig. 5(b). When single-probe measurement is used to measure the internal temperatures and only one temperature reading is taken for all 19 internal nodes in Fig. 5(c), the reconstruction errors shown in Fig. 5(e) are close to the previous ones in Fig. 5(d) where the low-fidelity measurement was taken and different nodal values were used in reconstruction, because the temperature gradient within this measured region is small.

In classical CS, depending on the reconstruction algorithms, the minimum number of measurement is in an order between $K\log(N/K)$ and K, which is associated with the level of sparsity K. In PBCS, the number of measurements can be reduced based on a prior knowledge of the physical system. For instance, in the example in Fig. 4, the number of measurements can be reduced to only two single-probe measurements, i.e. hotbed and extruder. Based on the knowledge of the system to be modeled, multiple nodes can be assigned to have the same temperature value. The physics based approach thus reduces the number of sensors to be deployed. Nevertheless, the strategy of reducing the number of sensors and designing locations of measurements could affect the reconstruction results.

5.2. *Monitoring 3D thermal distribution*

Here, the PBCS approach to monitor the printing process corresponding to the first physical experiment described in Section 4 is demonstrated. Fig. 6 shows a 3D model of the printed part, where four newly printed lines form a separate segment attached on the top left of the part. The dimension of each printed line is 0.75 mm × 45 mm × 1 mm. The extruder is currently at the location (3, 0, 6). Convection boundary conditions are applied to faces F1 to F4 and F6. Heat flux from the hotbed goes through face F5. Conduction matrix $\mathbf{K}_s$ in Eq. (7) is generated with $h_c = 25\,\mathrm{W{\bullet}m^{-2}{\bullet}K}$ and $\kappa = 0.1\,\mathrm{W{\bullet}m^{-2}{\bullet}K}$. The density of the material is $1.04\,\mathrm{g{\cdot}cm^{-3}}$, and the heat capacity is $1420\,\mathrm{J{\cdot}kg^{-1}{\cdot}K}$. A 3D mesh model is generated and the maximum mesh size is 8 mm, which is the length of the longest edge in the quadratic tetrahedral element. There are a total of 346 elements and 787 nodes.

In the first example, the PBCS reconstruction is based on the single-probe measurement, where one temperature reading on each of side faces F1 to F4 and top face of the newly printed segment F11 is taken to reconstruct the complete 3D temperature distribution. From the experimental measurement, 127 °C, 103 °C, 88 °C, and 82 °C are the temperature readings sampled at the center of each boundary edge from the thermal image in Fig. 1(b), which are labeled by dots in Fig. 7(a). They are assigned as the temperatures of all nodes on the side faces F1 to F4 respectively in the physical model. 140 °C is measured at the center of the top face formed by the newly printed segment and assigned as the nodal temperatures of face F11. The reconstructed 3D temperature distribution is shown in Fig. 7(b). Since the true 3D temperature distribution cannot be measured directly, the error associated with the PBCS reconstruction is unknown. To have an approximated estimation of the reconstruction error from the single-probe measurement, a baseline reconstruction is also performed, where the 2D

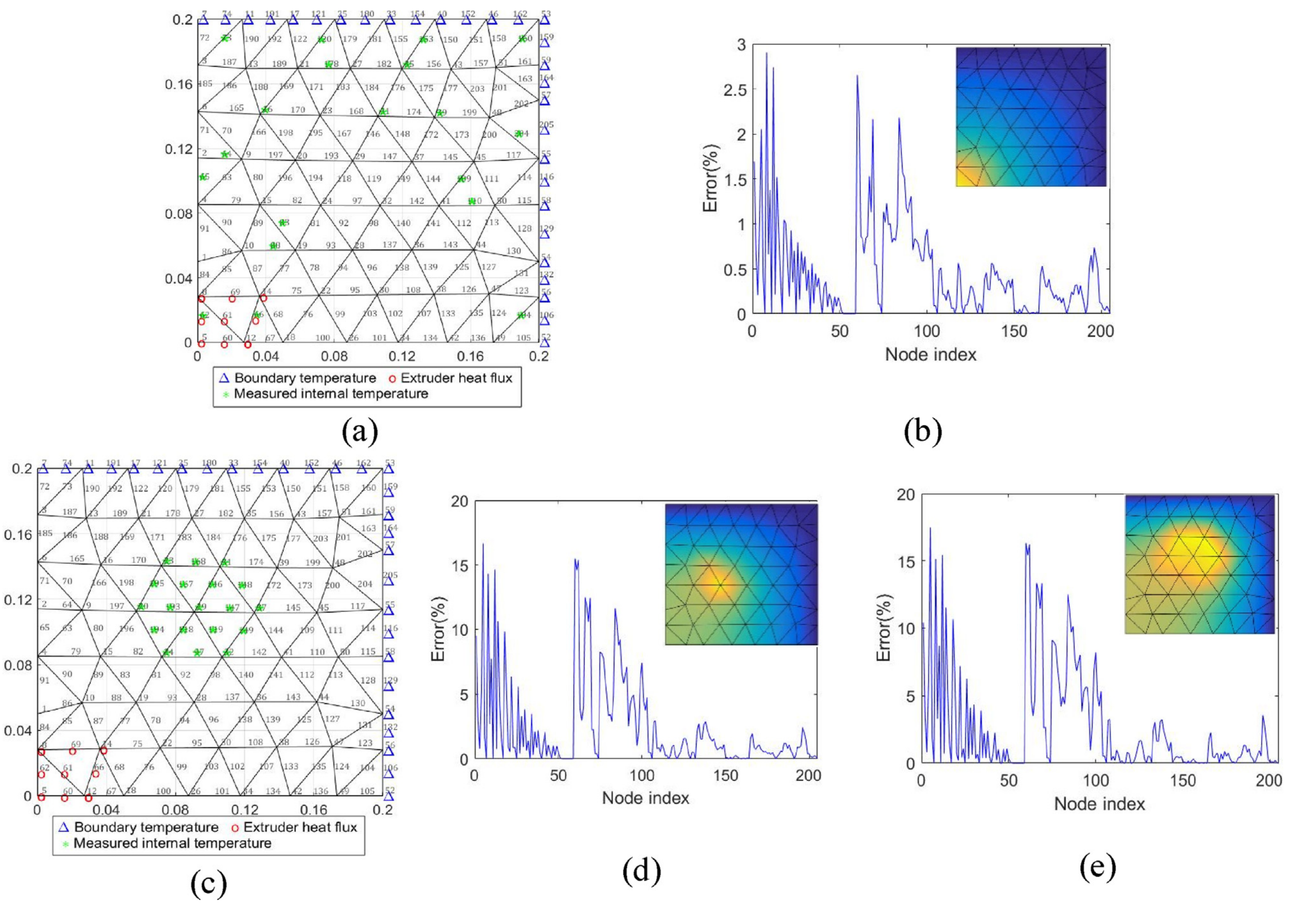

Fig. 5. Effects of measurement strategies. (a) Scattered internal temperature measurements in °C; (b) Reconstruction errors from (a) at the nodal positions with the basis pursuit algorithm; (c) Concentrated internal temperature measurements in °C; (d) Reconstruction errors from (c) at the nodal positions with the basis pursuit algorithm; (e) Reconstruction errors when the single-probe measurement is taken for internal temperatures instead in (c) with the basis pursuit algorithm.

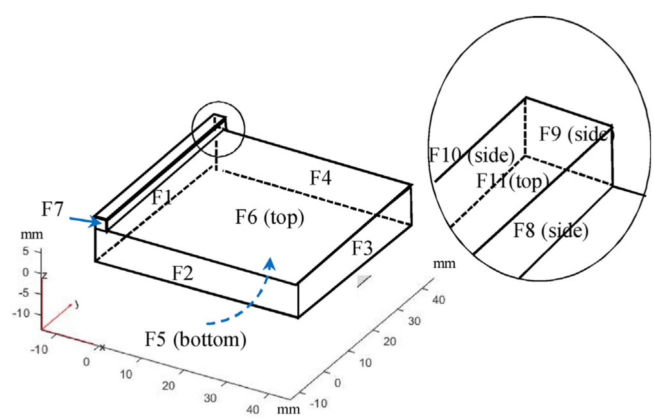

Fig. 6. The printing domain in material extrusion process.

temperature distribution on the top faces F6 and F11 from the experiment in Fig. 7(a) is used to assign the nodal temperatures on these two faces in the model for reconstruction. In other words, the nodes on these two faces take the actual temperatures respectively. The reconstructed baseline 3D temperature distribution is shown in Fig. 7(c). The temperature differences of all 787 nodes between PBCS reconstruction with the single-probe measurement and the baseline 3D distribution are shown in Fig. 7(d). The average error indicated by the dash line is 5.78% and the standard deviation of errors is 6.41%. To some extent the differences indicate the PBCS reconstruction error, although the ground truth is unknown. In the single-probe measurement, the compression ratio is 787/5 = 157.4. Here, OMP algorithm [14] is used for recovery. Our test also showed that the compression ratio is about 3 if classical CS is used to recover those nodal temperatures with the level of sparsity in the thermal load vector.

To compare the PBCS reconstruction with the direct full measurements of 2D temperature distribution from the thermal camera, the nodal temperatures on the top surfaces F6 and F11 from PBCS prediction are extracted. A 2D linear interpolation based on the nodal temperatures on F6 and F11 is used to store the temperature distribution as a matrix similar to an image. The size of the interpolated image from PBCS reconstruction is 45 × 45 pixels, which has the same size as the directly measured image in Fig. 7(a). The temperatures between the two images then are compared pixel by pixel. The differences are the PBCS sensing errors and are plotted with respect to x and y coordinates of pixels in Fig. 7(e). The average error is 6.86% and the standard deviation is 7.03%. Most errors come from face F11, where the temperature gradient is high in this small region. Assigning one temperature value to all nodes is not a good approximation. Adding more measurements can improve accuracy further. Neverthess, with the one temperature on F11, the reconstructed temperature distribution on face F6 is fair. The average and standard deviation of errors excluding F11 are 5.72% and 5.02%. Note that the whole domain of print is of interest because the complete thermal history is important to monitor the materials' phase transformation process.

A second example is to illustrate that more experimental measurements can reduce the reconstruction error. Based on the first example of the single-probe measurement, more temperature readings are taken from faces F6 and F11. The reconstructed 3D temperature distribution can be closer to the baseline reconstruction. The 2D domain of faces F6 and F11 is divided into several regions along x-direction, as shown in

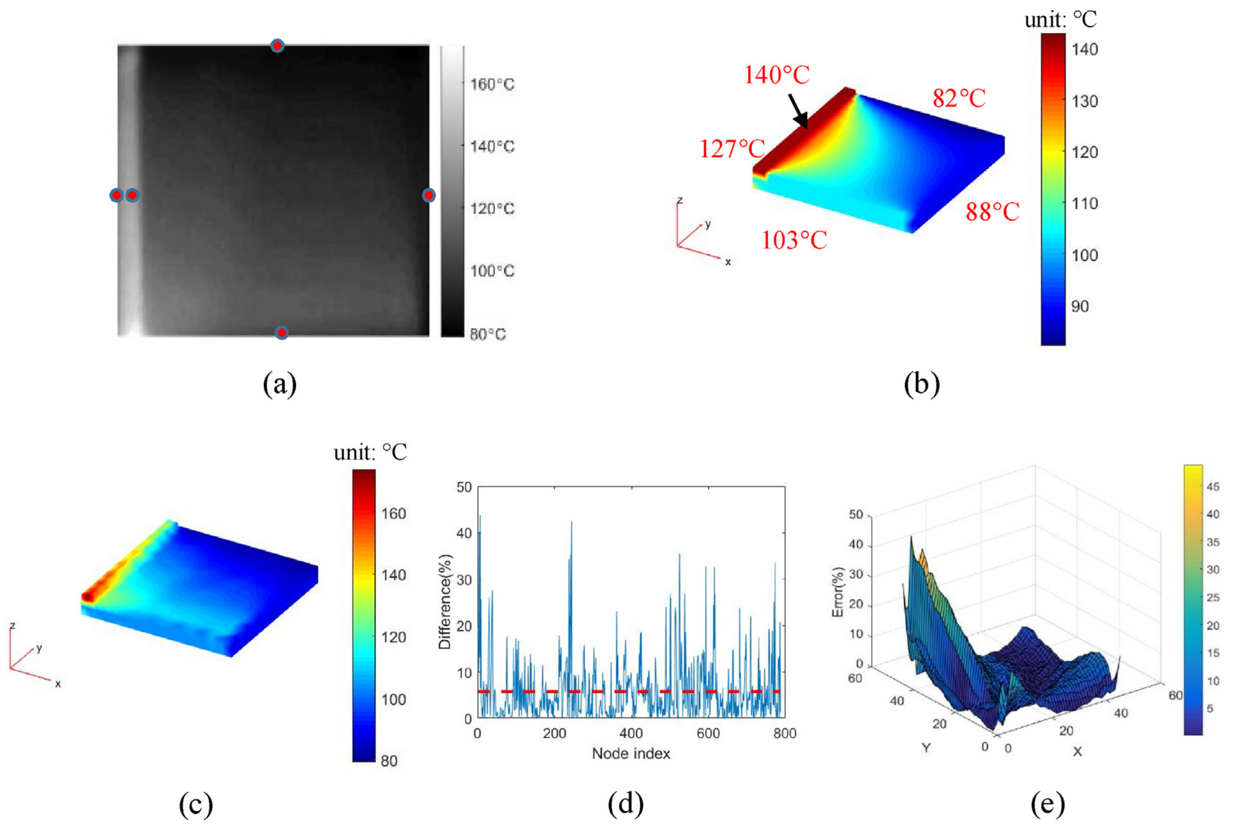

Fig. 7. PBCS reconstruction of 3D temperature distribution from the single-probe measurement. (a) 2D temperature field of top surface from the experimental measurement; (b) Reconstructed 3D temperature distribution from four side surface readings and one reading on face F11; (c) Baseline 3D reconstruction based on top surface temperature distributions and four side surface temperatures; (d) Temperature differences of all nodes between reconstruction from the single-probe measurement and the baseline reconstruction; and (e) Pixel-by-pixel differences between PBCS reconstructed top surface temperature distribution and the direct measurement from camera.

Fig. 8(a). The region enclosed by a box is the newly printed segment as face F11, which has much higher temperatures than other regions. Face F6 is further subdivided into different regions. One temperature reading at the center of bottom and top edges for each region is taken and is assigned to all nodes on bottom and top edges. Nodal temperatures along y-direction are then assigned by linearly interpolating temperatures on edges. In Fig. 8(b), the reconstructed 3D temperature distribution is based on four temperature readings from faces F1 to F4, two readings from face F11, and two readings from face F6 without further subdivision. The average nodal temperature difference between the reconstruction with a total of 8 measurements and the baseline is 5.68%, and the standard deviation is 5.64%, as shown in Fig. 8(c). It is seen that the errors are reduced from the ones in Fig. 7(d). The compression ratio for 8 measurement readings is 787/8 = 98.38. In Fig. 8(d,e), measurements include four temperature readings from faces F1 to F4, two readings from face F11, and twelve readings from face F6, where face F6 is further divided into six regions. In Fig. 8(f,g), a total of ninety readings are taken for reconstruction, including eighty-four readings from faces F6, where face F6 is divided into forty-two regions. The average differences are 4.39% and 3.94% respectively and the corresponding standard deviations are 4.26% and 3.48%.

5.3. Monitoring 3D transient temperature

For the transient process where temperature changes, temperature distribution $\boldsymbol{T}_k$ at time step k can be estimated based on the previous temperature distribution $\boldsymbol{T}_{k-1}$ at time step $k-1$, the time step τ, the mass matrix $\mathbf{M}$, the conduction matrix $\mathbf{K_s}$, and the heat load vector $\boldsymbol{L}$. This is according to their relationship expressed as

$$\boldsymbol{T}_k = \mathbf{A}\boldsymbol{T}_{k-1} + \mathbf{B}\boldsymbol{L} \tag{8}$$

where $\mathbf{A} = (\mathbf{M} + \tau\mathbf{K}_s)^{-1}\bullet\mathbf{M}$ and $\mathbf{B} = (\mathbf{M} + \tau\mathbf{K}_s)^{-1}\tau$.

Therefore, the constraint in Eq. (7) becomes

$$\boldsymbol{y}^* = \mathbf{\Phi}(\boldsymbol{T}_k - \mathbf{A}\boldsymbol{T}_{k-1}) = \mathbf{\Phi}\mathbf{B}\boldsymbol{L} \tag{9}$$

From measurements $\boldsymbol{y}^*$ for time steps $k-1$ and k, the sparse heat load vector $\boldsymbol{L}$ can be recovered. Then $\boldsymbol{T}_k$ can be reconstructed based on $\boldsymbol{T}_{k-1}$. Within a unit time step, the geometry of the model remains unchanged and the heating environment is steady. Therefore, $\boldsymbol{L}$, $\mathbf{M}$, and $\mathbf{K}_s$ will remain constant for each time step. Eq. (9) can be used for multiple time steps to reconstruct temperatures in the complete transient process.

In the second experiment described in Section 4, the printer is paused and the temperature distribution needs to be monitored. For the 3D model, same boundary conditions, the heat transfer coefficient, the conductivity and material properties are used as the static model in Section 5.2. The temperature distributions at different time steps can be reconstructed recursively using Eq. (9). The temperatures at three time steps, 0 s, 4 s, and 8 s, after the printer is paused are to be reconstructed. Temperature distribution $\boldsymbol{T}_2$ of time 8 s is reconstructed based on some measurements at time 8 s and $\boldsymbol{T}_1$ of time 4 s, whereas $\boldsymbol{T}_1$ of time 4 s is based on some measurements at time 4 s and $\boldsymbol{T}_0$ of time 0 s. However, in order to reconstruct $\boldsymbol{T}_0$ using Eq. (9), some temperature information prior to time 0 s is required, in addition to measurements at time 0 s. Here, the temperature distribution prior to time 0 s, denoted as $\boldsymbol{T}_{-1}$, is assumed to have a uniform value of 93 °C. Since the single-probe measurements of faces F1 to F4 are 95 °C, 86 °C, 87 °C, and 92 °C respectively at time 0 s, and the temperature of the newly printed segment is measured at the center of face F11 as 100 °C, the average of lower bound 86 °C and upper bound 100 °C thus is taken as the prior

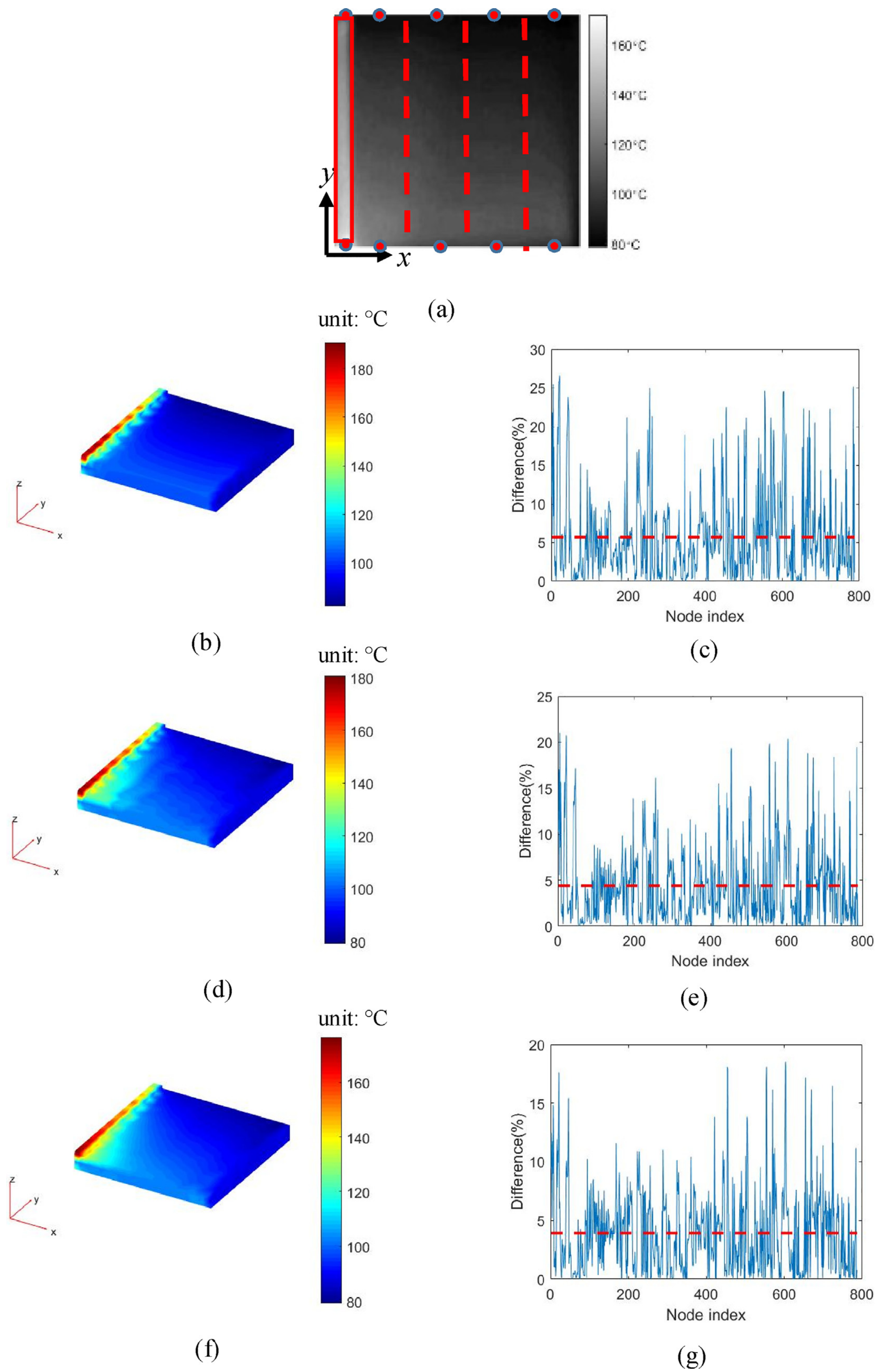

Fig. 8. Nodal temperature errors associated with the PBCS reconstructions are reduced when more measurements are taken. (a) Top faces F6 and F11 are subdivided into regions with two readings in each; (b) Reconstruction from 4 readings on faces F1 to F4 and 4 on top faces F6 and F11, and (c) the nodal temperature errors; (d) Reconstruction from 4 readings on faces F1 to F4 and 14 on top faces F6 and F11, and (e) the nodal temperature errors; (f) Reconstruction from 4 readings on faces F1 to F4 and 86 on top faces F6 and F11, and (g) the nodal temperature errors.

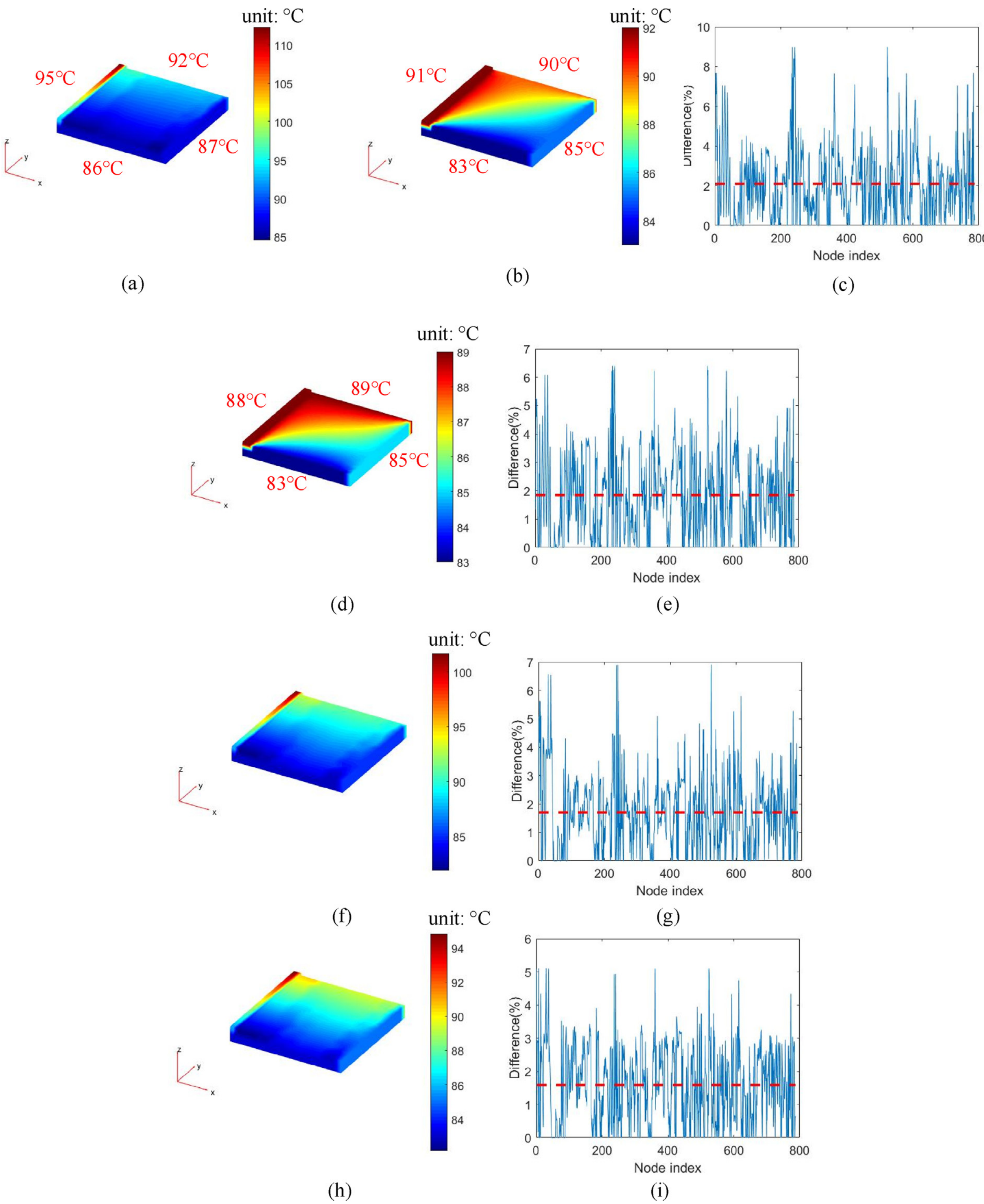

Fig. 9. Reconstructed temperature distributions and differences between PBCS reconstructions and baseline reconstructions for cooling. (a) Reconstructed 3D distributions at time 0 s. (b) Reconstruction with 5 readings on faces F1 to F4 and F11 and (c) nodal temperature differences compared to baseline construction at time 4 s; (d) Reconstruction with 5 readings on faces F1 to F4 and F11 and (e) nodal temperature differences compared to baseline construction at time 8 s; (f) Reconstruction with 18 readings and (g) nodal temperature differences at time 4 s; (h) Reconstruction with 18 readings and (i) nodal temperature differences at time 8 s.

information $\boldsymbol{T}_{-1}$. A total of 18 measurements including 4 readings on faces F1 to F4, 2 readings on face F11 and 12 readings on face F6 similar to the ones in Fig. 8(c) at time 0 s are used for PBCS reconstruction of $\boldsymbol{T}_0$, in addition to $\boldsymbol{T}_{-1}$. The reconstructed $\boldsymbol{T}_0$ at time 0 s is shown in Fig. 9(a). OMP is also used as the recovery algorithm.

Based on the reconstructed $\boldsymbol{T}_0$ and 5 single-probe measurements at faces F1 to F4 and F11 at time 4 s, $\boldsymbol{T}_1$ for time 4 s is reconstructed, as shown in Fig. 9(b). Similarly, with reconstructed $\boldsymbol{T}_1$ and single-probe measurements at time 8 s, temperature distribution $\boldsymbol{T}_2$ at time 8 s is further reconstructed, shown in Fig. 9(d). For accuracy assessment, similar to the static examples in Section 5.2, baseline reconstructions are performed based on the actual temperatures on top surfaces F6 and F11 and four single-probe measurements at side faces for time 4 s and 8 s. The nodal temperature differences between the baseline reconstructions and the single-probe reconstructions are shown in Fig. 9(c) and (e) respectively. When more readings are taken for reconstruction, the accuracy can improve. In Fig. 9(f) and (h), 4 readings from faces F1 to F4 and 14 readings on top faces F6 and F11, similar to Fig. 8(d), are used in the reconstructions at time 4 s and 8 s respectively. Their comparisons with baseline constructions are shown in Fig. 9(g) and (i). The reconstruction with 18 readings is better than the one with 5 readings at each time step.

It is also seen that the transient temperature reconstruction is more accurate than the static case in Section 5.2, because the correlation between time steps is taken into consideration and this additional information is useful. In addition, the range of the temperature values observed in this example is narrower than the one in the static case, where the temperature gradient on each face was larger. Therefore, for more uniformed temperature distributions with smaller gradients, single-probe temperature readings are closer to the actual temperatures, and the temperature reconstruction accuracy is higher.

The PBCS predicted top surface temperatures are also compared with the directly measured temperature fields by camera. The pixel-by-pixel differences are given in Fig. 10. In Fig. 10(a) and (b), the pixel-by-pixel differences for time 4 s and 8 s are shown, where 5 temperature readings are used for reconstruction at each time step. In Fig. 10(c) and (d), the differences for time 4 s and 8 s are shown, where 18 temperature readings are used for reconstruction at each time step. The average errors for them are 2.45% at 4 s and 2.23% at 8 s for 5 readings, and 1.91% and 1.99% for 18 readings respectively. The corresponding standard deviations of these errors are 1.43%, 1.27%, 0.96%, and 1.001%. It is seen that most errors come from the newly printed segment.

The PBCS errors can come from several sources. First, the accuracy of the physical model is important. The error in the physical model prediction becomes the bias inherited by PBCS reconstruction. For instance, during the 3D printing process, geometry may change because of the phase transition and shrinkage. The model built for PBCS reconstruction may not capture the variation of geometry. The mesh model is used as an approximation of PDE solutions. The discretization may also introduce model errors. In most cases, the transient model could be more accurate than the steady state model, since the correlation between measurements at different time steps is incorporated in reconstruction. Second, the error associated with experimental measurements is inherent in sensors, which is a part of PBCS error. During comparison, the numerical error from image registration and interpolation of nodal temperatures can contribute to the differences. Finally, the numerical error during the heat load vector recovery stage can also be part of the overall PBCS error.

6. Concluding remarks

In this paper, a novel approach to efficiently monitor the temperature distribution of manufacturing processes is proposed, where temperature information can be obtained from limited sensor data by incorporating physical models of heat transfer and numerical methods in compressive sensing. Compared to the traditional compressive sensing, the proposed physics based compressive sensing can significantly

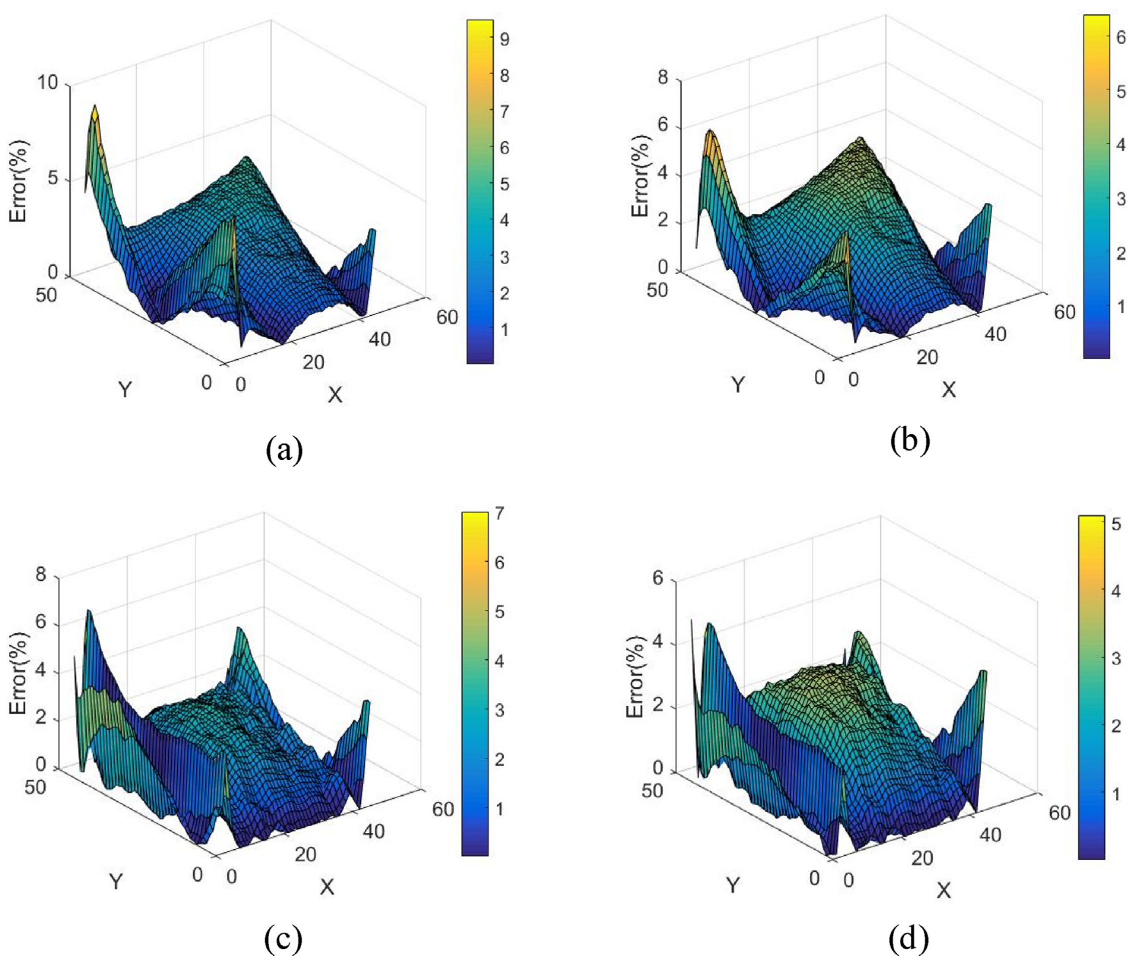

Fig. 10. Pixel-by-pixel comparison between PBCS predicted top surface temperature and registered image from camera. Differences at (a) time 4 s and (b) time 8 s with a total of 5 temperature readings for simultaneous reconstruction; Differences at (c) time 4 s and (d) time 8 s with a total of 18 temperature readings for simultaneous reconstruction.

improve the compression ratio and use low-cost sensors to replace high-cost ones. In experiments, it is demonstrated that only a few measurements for temperatures in the 3D printing domain, such as the side faces and a few readings on top faces in the printed part, are necessary to reconstruct the complete 3D temperature distribution. With less amount of data collected and fewer sensors deployed, the proposed physics-based compressive sensing shows its advantages over traditional compressed sensing for the process monitoring.

The proposed physics-based compressive sensing scheme has a good potential to significantly improve the efficiency of the manufacturing process monitoring with reduced system costs. In large-scale manufacturing systems with a variety of sensors, the proposed sensing and monitoring approach can be used to reduce the numbers as well as the types of sensors without losing much process information. In this way, the risk of sensor failure and the negative effect of undetected faulty sensors can be minimized.

The proposed PBCS approach for temperature measurement can be applied to measure both steady state and transient distributions. The major portion of PBCS error is from physical modeling. If more precise models are used in PBCS reconstruction, the errors can be reduced.

In future work, the physical models of the temperature distribution in additive manufacturing processes will be extended to incorporate more complex procedures such as thermal cycle in material extrusion and laser based powder bed fusion. Multi-physics models that consider the thermal expansion and shrinkage during manufacturing processes will be developed to improve the accuracy. The optimization scheme to find the best locations of sensors, especially for distributions with high gradients, will be developed so that the prediction error can be reduced. Different recovery algorithms used in traditional CS also need to be compared to assess their effectiveness in the new PBCS scheme.

Acknowledgments

Authors would like to thank Professor Jianjun Shi and Xiaolei Fang for their generous assistance in experiments.

References

[1] Candes EJ, Tao T. Near-optimal signal recovery from random projections: universal encoding strategies? IEEE Trans Inf Theory 2006;52(12):5406–25.
[2] Donoho DL. Compressed sensing. IEEE Trans Inf Theory 2006;52(4):1289–306.
[3] Baraniuk RG. Compressive sensing. IEEE Signal Process Mag 2007;24(4).
[4] Eldar YC, Kutyniok G, editors. Compressed sensing: theory and applications. Cambridge University Press; 2012.
[5] Lustig M, Donoho D, Pauly JM. Sparse MRI: the application of compressed sensing for rapid MR imaging. Magn Reson Med 2007;58(6):1182–95.
[6] Duarte MF, Davenport MA, Takhar D, Laska JN, Sun T, Kelly KE, Baraniuk RG. Single-pixel imaging via compressive sampling. IEEE Signal Process Mag 2008;25(2):83.
[7] Gan L. Block compressed sensing of natural images. 2007 IEEE 15th International Conference on Digital Signal Processing. 2007. p. 403–6.
[8] Haupt J, Bajwa WU, Rabbat M, Nowak R. Compressed sensing for networked data. IEEE Signal Process Mag 2008;25(2):92–101.
[9] Chen SS, Donoho DL, Saunders MA. Atomic decomposition by basis pursuit. SIAM Rev 2001;43(1):129–59.
[10] Tibshirani R. Regression shrinkage and selection via the lasso. J R Stat Soc Ser B (Methodol) 1996:267–88.
[11] Efron B, Hastie T, Johnstone I, Tibshirani R. Least angle regression. Annals Stat 2004;32(2):407–99.
[12] Recht B, Fazel M, Parrilo PA. Guaranteed minimum-rank solutions of linear matrix equations via nuclear norm minimization. SIAM Rev 2010;52(3):471–501.
[13] Mallat SG, Zhang Z. Matching pursuits with time-frequency dictionaries. IEEE Trans Signal Process 1993;41(12):3397–415.
[14] Tropp JA, Gilbert AC. Signal recovery from random measurements via orthogonal matching pursuit. IEEE Trans Information Theory 2007;53(12):4655–66.
[15] Needell D, Vershynin R. Uniform uncertainty principle and signal recovery via regularized orthogonal matching pursuit. Found Comput Math 2009;9(3):317–34.
[16] Donoho DL, Tsaig Y, Drori I, Starck JL. Sparse solution of underdetermined systems of linear equations by stagewise orthogonal matching pursuit. IEEE Trans Information Theory 2012;58(2):1094–121.
[17] Needell D, Tropp JA. CoSaMP: iterative signal recovery from incomplete and inaccurate samples. Appl Comput Harmon Anal 2009;26(3):301–21.
[18] Dai W, Milenkovic O. Subspace pursuit for compressive sensing signal reconstruction. IEEE Trans Inf Theory 2009;55(5):2230–49.
[19] Nowak RD, Wright SJ. Gradient projection for sparse reconstruction. IEEE J Select Topics Signal Process 2007;1(4):586–97.
[20] Liu E, Temlyakov VN. The orthogonal super greedy algorithm and applications in compressed sensing. IEEE Trans Inf Theory 2012;58(4):2040–7.
[21] Donoho DL. De-Noising by soft-thresholding. IEEE Trans Inf Theory 1995;41(3):613–27.
[22] Blumensath T, Davies ME. Iterative hard thresholding for compressed sensing. Appl Comput Harmon Anal 2009;27(3):265–74.
[23] Berinde R, Indyk P, Ruzic M. Practical near-optimal sparse recovery in the l1 norm 2008, September 46th Annual Allerton Conference on Communication, Control, and Computing2008. p. 198–205.
[24] Berinde R, Indyk P. Sequential sparse matching pursuit 2009, September 47th Annual Allerton Conference on Communication, Control, and Computing2009. p. 36–43.
[25] Gilbert AC, Muthukrishnan S, Strauss M. Improved time bounds for near-optimal sparse Fourier representations 2005, August Opt Photon2005. 59141A-59141A.
[26] Gilbert AC, Strauss MJ, Tropp JA, Vershynin R. One sketch for all: fast algorithms for compressed sensing 2007, June ACM Proceedings of the Thirty-Ninth Annual ACM Symposium on Theory of Computing. 2007. p. 237–46.
[27] Chartrand R. Exact reconstruction of sparse signals via nonconvex minimization. IEEE Signal Process Lett 2007;14(10):707–10.
[28] Murray JF, Kreutz-Delgado K. An improved FOCUSS-based learning algorithm for solving sparse linear inverse problems 2001, November Conference Record of the Thirty-Fifth Asilomar Conference on Signals, Systems and Computers, vol. 1. 2001. p. 347–51.
[29] Wotao Y, Stanley O, Donald G, Jerome D. Bregman iterative algorithms for l1-minimization with applications to compressed sensing. SIAM J Imag Sci 2008;1(1):143–68.
[30] Chen X, Du Z, Li J, Li X, Zhang H. Compressed sensing based on dictionary learning for extracting impulse components. Signal Process 2014;96:94–109.
[31] Wang Y, Xiang J, Mo Q, He S. Compressed sparse time–frequency feature representation via compressive sensing and its applications in fault diagnosis. Measurement 2015;68:70–81.
[32] Wang H, Ke Y, Luo G, Tang G. Compressed sensing of roller bearing fault based on multiple down-sampling strategy. Meas Sci Technol 2015;27(2):025009.
[33] Tang G, Yang Q, Wang HQ, Luo GG, Ma JW. Sparse classification of rotating machinery faults based on compressive sensing strategy. Mechatronics 2015;31:60–7.
[34] Ding X, He Q. Time–frequency manifold sparse reconstruction: a novel method for bearing fault feature extraction. Mech Syst Signal Process 2016;80:392–413.
[35] Yuan H, Lu C. Rolling bearing fault diagnosis under fluctuant conditions based on compressed sensing. Struct Control Health Monit 2016;24(5):e1918.
[36] Liu C, Wu X, Mao J, Liu X. Acoustic emission signal processing for rolling bearing running state assessment using compressive sensing. Mech Syst Signal Process 2016;91:395–406.
[37] Guo L, Gao H, Li J, Huang H, Zhang X. Machinery vibration signal denoising based on learned dictionary and sparse representation. J Phys: Conf Ser 2015;vol. 628(1):012124.
[38] Zhou H, Chen J, Dong G, Wang R. Detection and diagnosis of bearing faults using shift-invariant dictionary learning and hidden Markov model. Mech Syst Signal Process 2016;72:65–79.
[39] Ozisik MN. Inverse heat transfer: fundamentals and applications. CRC Press; 2000.
[40] Park HM, Yoon TY. Solution of the inverse radiation problem using a conjugate gradient method. Int J Heat Mass Transfer 2000;43(10):1767–76.
[41] Chantasiriwan S. Inverse heat conduction problem of determining time-dependent heat transfer coefficient. Int J Heat Mass Transfer 1999;42(23):4275–85.
[42] Su J, Hewitt GF. Inverse heat conduction problem of estimating time-varying heat transfer coefficient. Numer Heat Transf Part A: Appl 2004;45(8):777–89.
[43] Huang CH, Chiang CC, Chen HM. Shape identification problem in estimating geometry of multiple cavities. J Thermophys Heat Transfer 1998;12(2):270–7.
[44] Huang CH, Ozisik MN, Sawaf B. Conjugate gradient method for determining unknown contact conductance during metal casting. Int J Heat Mass Transfer 1992;35(7):1779–86.
[45] Liu FB. A modified genetic algorithm for solving the inverse heat transfer problem of estimating plan heat source. Int J Heat Mass Transfer 2008;51(15-16):3745–52.